High-order lattice-Boltzmann model for the Cahn-Hilliard equation

Chunhua Zhang and Zhaoli Guo*
State Key Laboratory of Coal Combustion, Huazhong University of Science and Technology, Wuhan 430074, China

Hong Liang
Department of Physics, Hangzhou Dianzi University, Hangzhou 310018, China

(Received 26 September 2018; revised manuscript received 26 March 2019; published 30 April 2019)

The Cahn-Hilliard equation (CHE) is widely used in modeling two-phase fluid flows, and it is critical to solve this equation accurately to track the interface between the two phases. In this paper, a high-order lattice Boltzmann equation model is developed for the CHE via the fourth-order Chapman-Enskog expansion. A truncation error analysis is performed, and the leading error term proportional to the Peclet number is identified. The results are further confirmed by the Maxwell iteration. With the inclusion of a correction term for eliminating the main error term, the proposed model is able to recover the CHE up to third order. The proposed model is tested by several benchmark problems. The results show that the present model is capable of tracking the interface with improved accuracy and stability in comparison with the second-order one.

DOI: 10.1103/PhysRevE.99.043310

I. INTRODUCTION

Two-phase flows with complex interfacial dynamics appear in many fields of science and engineering applications. It is important to develop effective and accurate numerical methods for simulating such flows. In the designing of numerical methods, it is critical to describe the motion of fluid interface accurately. Generally, the existing numerical methods for multiphase flows can be divided into two categories, i.e., sharp interface methods [1,2] and diffuse interface methods [3–7]. In a sharp interface method, the fluid interface is treated as a sharp discontinuity with zero thickness that separates the two fluids. The hydrodynamics of each fluid is described by the individual governing equations, which can be solved by some standard numerical techniques. In such methods, the interface just serves as a moving boundary with compatible conditions through which the effects of interfacial properties on the flow are incorporated. Therefore, it is critical to capture accurately the change and motion of the interface in sharp-interface methods. In a diffuse interface method, the interface is replaced by a transition region of small but finite width, across which density, viscosity, and other physical quantities of the two-phase fluids vary smoothly. The hydrodynamics of the whole system is described by a single set of governing equations [Navier-Stokes (NS) equations] with a body force term accounting for the interfacial force, which can be modeled based on surface tension (continuum surface force model) or fluid free-energy (phase-field model). In the latter case, the motion and topological change of the interface can be described by the evolution of an order parameter governed by a phase-field equation, such as the Cahn-Hilliard equation (CHE) [3,8,9] or the Allen-Cahn equation (ACE) [10–12]. Compared with sharp interface methods, diffuse interface methods have some advantages in simulating interface movement and deformation on fixed grids [5,13]. For example, diffuse interface methods enable us to compute the interface without explicitly tracking it, and we can resolve interface curvature with higher accuracy.

Numerical methods based on diffuse interface methods have attracted much interest in recent years. Among these, the lattice Boltzmann equation (LBE) method has gained much success due to its simplicity and efficiency [14–20]. In such LBE models, two sets of distribution functions are used. One is employed to solve the phase-field equation (CHE or ACE) and the other is used to solve the hydrodynamic equations. The LBE for the Navier-Stokes equations is standard, but the LBE for the phase-field equation is nontrivial. To recover the phase-field equation correctly, some models have been developed for both CHE and ACE. The first attempt to devise a LBE describing the evolution of a phase-field variable is due to He *et al.* [21], who reproduced an equation similar to the CHE but with some explicit differences. Later, Zheng *et al.* [7] proposed a modified version with a spatial difference term of the distribution function such that the CHE can be recovered exactly. Following the same strategy, Zu *et al.* [22] replaced the distribution function with the equilibrium one in the spatial difference term to improve the numerical stability. Recently, Liang *et al.* [18] introduced a time-derivative term in the their LBE model to ensure that the CHE can be recovered correctly. In addition to recovering the CHE, some LBE models for the Allen-Cahn equation have also been developed to track the interface between two different fluids [23–26]. For instance, Geier *et al.* [23] developed a central-moment LBE model for the ACE; Fakhari *et al.* [25] employed a finite-difference LBE model for the ACE to facilitate the use of nonuniform grids; and recently a LBE model with a time-derivative source term was proposed to recover the ACE exactly [26].

However, all of the above LBE models for the CHE or ACE are based on a second-order Chapman-Enskog analysis

*zlguo@hust.edu.cn

[7,18,22,26]. All higher-order terms than the second-order term that may be important near the interface are neglected. To the best of our knowledge, no theoretical analysis of the influence of these error terms is available for the CHE. However, some efforts have been made by a high-order Chapman-Enskog expansion to remove some high-order error terms partially in terms of the advection-diffusion equation and Navier-Stokes equations [27–33]. In this paper, we shall perform a truncation error analysis of the LBE model using the fourth-order Chapman-Enskog expansion. It turns out that the truncation error should not be completely neglected through the dimensionless analysis. To improve the accuracy of the LBE model, a correction term is proposed to remove the leading error. In addition, the results are further confirmed by the Maxwell iteration method that need not explicitly introduce multiple-scale variables [34,35].

The rest of this paper is organized as follows. In Sec. II, a truncation error analysis is presented for the LBE model for the CHE via the higher-order Chapman-Enskog expansion, from which the moments of the source terms are determined. In Sec. III, some numerical simulations are carried out to validate the proposed model, and some comparisons with previous LBE models are made. A brief summary is presented in Sec. IV.

II. PHASE-FIELD LATTICE BOLTZMANN METHOD

A. Cahn-Hilliard equation

In phase-field theory for a two-phase system (denoted by A and B, respectively), an order parameter $\phi(\boldsymbol{x},t)$ is used to identify different fluid phases, e.g., ϕ_A denotes the bulk phase A and ϕ_B denotes the bulk phase B. The order parameter is closely related to the free energy of the system. For an isothermal binary fluid system, the free energy can be expressed as

$$F(\phi)=\int_V\left[f(\phi)+\frac{\kappa}{2}|\nabla\phi|^2\right]dV, \tag{1}$$

where $f(\phi)$ is the bulk free-energy density, κ is a constant related to surface tension, and V is the control volume. In general, the bulk free-energy density can be modeled as a double-well potential for pseudo–van der Waals fluids [4,36],

$$f(\phi)=\beta(\phi-\phi_A)^2(\phi-\phi_B)^2, \tag{2}$$

The two parameters κ and β related to the interfacial thickness W and the surface tension σ are given by [4,36]

$$\beta=\frac{12\sigma}{W|\phi_A-\phi_B|^4},\quad \kappa=\frac{3\sigma W}{2|\phi_A-\phi_B|^2}. \tag{3}$$

From the free energy of the system, one can define the chemical potential μ as follows

$$\mu\equiv\frac{\delta F}{\delta\phi}=\frac{\partial f}{\partial\phi}-\kappa\nabla^2\phi. \tag{4}$$

At equilibrium, the chemical potential is constant. In particular, for a planar interface the equilibrium distribution of the order parameter can be expressed as

$$\phi(z)=\frac{\phi_A+\phi_B}{2}+\frac{\phi_A-\phi_B}{2}\tanh\left(\frac{2z}{W}\right), \tag{5}$$

where z is the coordinate normal to the interface. The dynamics of the order parameter can be described by the CHE [8,37],

$$\frac{\partial\phi}{\partial t}+\nabla\cdot(\phi\boldsymbol{u})=\nabla\cdot(M\nabla\mu), \tag{6}$$

where M is the mobility and $\boldsymbol{u}$ is the fluid velocity governed by the incompressible Navier-Stokes equations [4,6,13,38,39],

$$\nabla\cdot\boldsymbol{u}=\boldsymbol{0}, \tag{7a}$$

$$\rho(\partial_t\boldsymbol{u}+\boldsymbol{u}\cdot\nabla\boldsymbol{u})=-\nabla p+\nabla\cdot\Pi+\boldsymbol{F}_s,\quad \text{or} \tag{7b}$$

$$\partial_t(\rho\boldsymbol{u})+\nabla\cdot(\rho\boldsymbol{u}\boldsymbol{u})=-\nabla p+\nabla\cdot\Pi+\boldsymbol{F}_s+\frac{d\rho}{d\phi}\boldsymbol{u}\nabla\cdot(M\nabla\mu), \tag{7c}$$

where ρ is the density, p is the pressure, $\Pi=\rho\nu(\nabla\boldsymbol{u}+\nabla\boldsymbol{u}^T)$ is the viscous stress tensor with ν being the kinematic viscosity, and $F_s=-\phi\nabla\mu$ is the surface tension force. The fluid density is determined by the order parameter

$$\rho=\frac{\phi-\phi_B}{\phi_A-\phi_B}(\rho_A-\rho_B)+\rho_B. \tag{8}$$

B. The LBE model for the Cahn-Hilliard equation

The LBE for the CHE with a single-time relaxation approximation is expressed as [16,18,40]

$$g_i(\boldsymbol{x}+\boldsymbol{c}_i\delta t,t+\delta t)-g_i(\boldsymbol{x},t)=-\frac{g_i(\boldsymbol{x},t)-g_i^{\rm eq}(\boldsymbol{x},t)}{\tau_g}+\delta t S_i(\boldsymbol{x},t), \tag{9}$$

where $g_i(\boldsymbol{x},\boldsymbol{c}_i,t)$ is the distribution function associated with discrete velocity $\boldsymbol{c}_i$ at position $\boldsymbol{x}$ and time t, δt is the time step, τ_g is the nondimensional relaxation time, $g_i^{\rm eq}$ is the equilibrium distribution function, and $S_i(\boldsymbol{x},t)$ is a source term to be determined later to ensure that the CHE is recovered correctly. In this study, we only consider two-dimensional problems, and the two-dimensional nine velocity (D2Q9) model is employed, in which the discrete velocities are given by $\boldsymbol{c}_0=(0,0)c$, $\boldsymbol{c}_1=-\boldsymbol{c}_3=(1,0)c$, $\boldsymbol{c}_2=-\boldsymbol{c}_4=(0,1)c$, $\boldsymbol{c}_5=-\boldsymbol{c}_7=(1,1)c$, and $\boldsymbol{c}_6=-\boldsymbol{c}_8=(-1,1)c$, with $c=\delta_x/\delta_t$ being the lattice speed (δ_x being the lattice spacing). To match the CHE correctly, the moments of the equilibrium distribution function should satisfy [18,25,40–42]

$$\sum_i g_i^{\rm eq}=\phi,\quad \sum_i\boldsymbol{c}_i g_i^{\rm eq}=\phi\boldsymbol{u},\quad \sum_i\boldsymbol{c}_i\boldsymbol{c}_i g_i^{\rm eq}=c_s^2\eta\mu\boldsymbol{I}+\bar{\boldsymbol{C}}, \tag{10}$$

where η is an adjustable parameter related to the mobility, c_s is the sound speed defined by $c_s=c/\sqrt{3}$, and $\bar{\boldsymbol{C}}$ is a function of velocity. In [18,22,25,41], $\bar{\boldsymbol{C}}=\boldsymbol{0}$ is used. In [16,19,40,42,43], $\bar{\boldsymbol{C}}=\phi\boldsymbol{u}\boldsymbol{u}$ is used. Here, the former is employed and the following equilibrium distribution function satisfying the above

moments is used [18]:

$$g_i^{\mathrm{eq}} = \begin{cases} \phi + (\omega_0 - 1)\eta\mu, & i = 0, \\ \omega_i \eta\mu + \omega_i \phi \frac{\boldsymbol{c}_i \cdot \boldsymbol{u}}{c_s^2}, & i \neq 0, \end{cases} \tag{11}$$

where ω_i is the weight coefficient defined by $\omega_0 = 4/9$, $\omega_{1-4} = 1/9$, and $\omega_{5-8} = 1/36$ in the D2Q9 model.

The source term S_i can be expressed as follows [44]:

$$S_i = \bar{\omega}_i C_0 + \omega_i \frac{\boldsymbol{c}_i \cdot \boldsymbol{B}}{c_s^2}, \tag{12}$$

where C_0 and $\boldsymbol{B}$ are undetermined parameters to recover the CHE with high-order accuracy, $\bar{\omega}_i$ are weight coefficients, and there are some constraints on $\bar{\omega}_i$,

$$\sum \bar{\omega}_i = 0, \quad \sum \bar{\omega}_i \boldsymbol{c}_i = 0, \quad \sum \bar{\omega}_i \boldsymbol{c}_i \boldsymbol{c}_i = c_s^2 \boldsymbol{I}. \tag{13}$$

Then, the zeroth through second moments of S_i are

$$\sum_i S_i = 0, \quad \sum_i \boldsymbol{c}_i S_i = \boldsymbol{B}, \quad \sum_i \boldsymbol{c}_i \boldsymbol{c}_i S_i = c_s^2 C_0 \boldsymbol{I}. \tag{14}$$

Finally, the order parameter is computed from the distribution function as follows (see Appendix A):

$$\phi = \sum g_i. \tag{15}$$

C. High-order analysis with the Chapman-Enskog expansion

In the framework of Chapman-Enskog analysis, the distribution function is expanded in a power series of a small parameter ϵ, which is of order of the Knudsen number (the ratio between the mean free path and a characteristic macroscopic length). It is noted that the value of the Knudsen number is small in the bulk phase while it may not be small near the interface. Thus, some high-order terms may not be completely neglected. The series expansion is expressed as

$$g_i = g_i^{(0)} + \epsilon g_i^{(1)} + \epsilon^2 g_i^{(2)} + \epsilon^3 g_i^{(3)} + \epsilon^4 g_i^{(4)} + \cdots, \tag{16}$$

where $g_i^{(1)}$, $g_i^{(2)}$, $g_i^{(3)}$, and $g_i^{(4)}$ represent the first through fourth approximation to the distribution function, respectively, and so on. Since the balance equation links space and time derivatives, these derivatives are also expressed in terms of multiple-scale variables ϵ [28,45]. Retaining the terms up to $O(\epsilon^4)$, we have

$$\begin{aligned} \nabla &= \epsilon \nabla_1, \quad \partial_t = \epsilon \partial_{t_1} + \epsilon^2 \partial_{t_2} + \epsilon^3 \partial_{t_3} + \epsilon^4 \partial_{t_4}, \\ S_i &= \epsilon S_i^{(1)} + \epsilon^2 S_i^{(2)} + \epsilon^3 S_i^{(3)} + \epsilon^4 S_i^{(4)}, \\ C_0 &= \epsilon C_0^{(1)} + \epsilon^2 C_0^{(2)} + \epsilon^3 C_0^{(3)} + \epsilon^4 C_0^{(4)}, \\ \boldsymbol{B} &= \epsilon \boldsymbol{B}^{(1)} + \epsilon^2 \boldsymbol{B}^{(2)} + \epsilon^3 \boldsymbol{B}^{(3)} + \epsilon^4 \boldsymbol{B}^{(4)}. \end{aligned} \tag{17}$$

The meaning of the symbols ∂_{t_1}, ∂_{t_2}, ∂_{t_3}, and ∂_{t_4} is that the recovered equations define ∂_t in terms of the spatial gradients of the moments and the definition of the distribution [46]. Generally speaking, ∂_{t_1} is considered as the convective timescale and ∂_{t_2} is the diffusion timescale. However, for the higher-order timescale, there is no well-defined physical name yet. Based on Eqs. (10), (15), (16), and (20), we can obtain

$$\sum_i g_i^{(n)} = 0, \quad n > 0. \tag{18}$$

Applying the Taylor expansion to Eq. (9) leads to

$$\delta t D_i g_i + \frac{\delta t^2}{2} D_i^2 g_i + \frac{\delta t^3}{6} D_i^3 g_i + \frac{\delta t^4}{24} D_i^4 g_i + \cdots = -\frac{g_i - g_i^{\mathrm{eq}}}{\tau_g} + \delta t S_i, \tag{19}$$

where $D_i = \partial_t + \boldsymbol{c}_i \cdot \nabla$. Substituting Eqs. (16) and (17) into Eq. (19) and dividing through by δt, the following equations at different orders of ϵ can be obtained:

$$\epsilon^0 \text{:}\ g_i^{(0)} = g_i^{\mathrm{eq}}, \tag{20}$$

$$\epsilon^1 \text{:}\ D_{1i} g_i^{(0)} = -\frac{1}{\tau_1} g_i^{(1)} + S_i^{(1)}, \tag{21}$$

$$\epsilon^2 \text{:}\ \partial_{t_2} g_i^{(0)} + D_{1i} g_i^{(1)} + \frac{\delta t}{2} D_{1i}^2 g^{(0)} = -\frac{1}{\tau_1} g_i^{(2)} + S_i^{(2)}, \tag{22}$$

$$\epsilon^3 \text{:}\ \partial_{t_3} g_i^{(0)} + \partial_{t_2} g_i^{(1)} + D_{1i} g_i^{(2)} + \frac{\delta t}{2} \partial_{t_2} D_{1i} g_i^{(0)} + \frac{\delta t}{2} D_{1i} \partial_{t_2} g^{(0)} + \frac{\delta t}{2} D_{1i}^2 g_i^{(1)} + \frac{\delta t^2}{6} D_{1i}^3 g_i^{(0)} = -\frac{1}{\tau_1} g_i^{(3)} + S_i^{(3)}, \tag{23}$$

$$\begin{aligned} \epsilon^4 \text{:}\ & \partial_{t_4} g_i^{(0)} + \partial_{t_3} g_i^{(1)} + \partial_{t_2} g_i^{(2)} + D_{1i} g_i^{(3)} + \frac{\delta t}{2} D_{1i}^2 g_i^{(2)} + \frac{\delta t}{2} \partial_{t_2} D_{1i} g_i^{(1)} + \frac{\delta t}{2} D_{1i} \partial_{t_2} g_i^{(1)} + \frac{\delta t}{2} \partial_{t_2}^2 g_i^{(0)} \\ & + \frac{\delta t}{2} \partial_{t_3} D_{1i} g_i^{(0)} + \frac{\delta t}{2} D_{1i} \partial_{t_3} g_i^{(0)} + \frac{\delta t^2}{6} D_{1i}^3 g_i^{(1)} + \frac{\delta t^2}{6} D_{1i}^2 \partial_{t_2} g_i^{(0)} + \frac{\delta t^2}{6} \partial_{t_2} D_{1i}^2 g_i^{(0)} \\ & + \frac{\delta t^2}{6} D_{1i} \partial_{t_2} D_{1i} g_i^{(0)} + \frac{\delta t^3}{24} D_{1i}^4 g_i^{(0)} = -\frac{1}{\tau_1} g_i^{(4)} + S_i^{(4)}, \end{aligned} \tag{24}$$

where $D_{1i} = \partial_{t_1} + \boldsymbol{c}_i \cdot \nabla_1$ and $\tau_1 = \tau_g \delta t$.

For the sake of simplicity, we briefly denote the moments of the equilibrium distribution function g^{eq} as

$$\pi_m^{(1)} = \sum_i g_i^{eq} c_{mi}, \quad \pi_{mn}^{(2)} = \sum_i g_i^{eq} c_{mi} c_{ni},$$
$$\pi_{mnl}^{(3)} = \sum_i g_i^{eq} c_{mi} c_{ni} c_{li}, \quad \pi_{mnl\theta}^{(4)} = \sum_i g_i^{eq} c_{mi} c_{ni} c_{li} c_{\theta i}, \tag{25}$$

where the subscripts m, n, l, θ denote Cartesian coordinates, and a summation over these repeated subscripted indices is assumed. With Eqs. (14), (18), and (25), taking the zeroth-order moment of Eqs. (21), (22), and (23) gives

$$\partial_{t_1}\phi = -\nabla_1 \cdot (\phi \boldsymbol{u}) + \mathrm{TE}_1, \tag{26a}$$
$$\partial_{t_2}\phi = M\nabla_1^2\mu + \mathrm{TE}_2, \tag{26b}$$
$$\partial_{t_3}\phi = \mathrm{TE}_3, \tag{26c}$$
$$\partial_{t_4}\phi = \mathrm{TE}_4, \tag{26d}$$

with the truncation errors (TEs) being

$$\mathrm{TE}_1 = \partial_m\big(\phi u_m - \pi_m^{(1)}\big), \tag{27}$$
$$\mathrm{TE}_2 = \partial_{mn}\big(\tau_2\pi_{mn}^{(2)} - M\mu\delta_{mn}\big) + \tau_2\partial_{t_1}\partial_m\pi_m^{(1)} - \tau_1\partial_m B_m^{(1)}, \tag{28}$$
$$\begin{aligned}\mathrm{TE}_3 = {} & \tau_2\big(\partial_{t_2t_1}\phi + \partial_{t_2}\partial_m\pi_m^{(1)} + \partial_{t_1t_2}\phi + \partial_{t_2}\partial_m\pi_m^{(1)}\big) + \tau_3\big(2\partial_{t_1}^2\partial_m\pi_m^{(1)} + 3\partial_{t_1}\partial_{mn}\pi_{mn}^{(2)} + \partial_{mnl}\pi_{mnl}^{(3)}\big)\\ & +\tau_1\tau_2\big(c_s^2\partial_{mn}C_0^{(1)}\delta_{mn} + 2\partial_{t_1}\partial_m B_m^{(1)}\big) - \tau_1\partial_m B_m^{(2)},\end{aligned} \tag{29}$$
$$\begin{aligned}\mathrm{TE}_4 = {} & \tau_4\big(\partial_{t_1}^4\phi + 4\partial_{t_1}^3\partial_m\pi_m^{(1)} + 6\partial_{t_1}^2\partial_{mn}\pi_{mn}^{(2)} + 4\partial_{t_1}\partial_{mnl}\pi_{mnl}^{(3)} + \partial_{mnl\theta}\pi_{mnl\theta}^{(4)}\big) + \tau_2\partial_{t_2}^2\phi\\ & +\tau_3\big(\partial_{t_2}\partial_{t_1}\partial_m\pi_m^{(1)} + \partial_{t_2}\partial_{mn}\pi_{mn}^{(2)}\big) + \tau_3\big(\partial_{t_1}^2\partial_{t_2}\phi + 2\partial_{t_1t_2}\partial_m\pi_m^{(1)} + \partial_{t_2}\partial_{mn}\pi_{mn}^{(2)}\big)\\ & +\tau_3\big(\partial_{t_1t_2t_1}\phi + \partial_{t_1t_2}\partial_m\pi_m^{(1)} + \partial_{t_2t_1}\partial_m\pi_m^{(1)} + \partial_{mn}\partial_{t_2}\pi_{mn}^{(2)}\big) + \tau_2\big(\partial_{t_1t_3}\phi + \partial_m\partial_{t_3}\pi_m^{(1)}\big)\\ & +\tau_1\tau_2\big(2\partial_{t_1}\partial_m B_m^{(2)} + c_s^2\partial_{mn}C_0^{(2)}\delta_{mn} + \partial_{t_2}\partial_m B_m^{(1)} + \partial_m\partial_{t_2}B_m^{(1)}\big) - \tau_1\partial_m B_m^{(3)}\\ & +\tau_1\tau_3\big(3\partial_m\partial_{t_1}^2 B_m^{(1)} + 3c_s^2\partial_{t_1}\partial_{mn}C_0^{(1)}\delta_{mn} + 3c_s^2\partial_m^2\partial_n B_n^{(1)}\big),\end{aligned} \tag{30}$$

and the abbreviated coefficient being

$$\tau_2 = \big(\tau_g - \tfrac{1}{2}\big)\delta t,$$
$$\tau_3 = \big(-\tau_g^2 + \tau_g - \tfrac{1}{6}\big)\delta t^2,$$
$$\tau_4 = \big(\tau_g^3 - \tfrac{3}{2}\tau_g^2 - \tfrac{7}{12}\tau_g + \tfrac{1}{24}\big)\delta t^3. \tag{31}$$

Note that the t_2 derivative of Eq. (26a) reads $\partial_{t_2}\partial_{t_1}\phi = -\partial_{t_2}\partial_m(\phi u_m)$ while the t_1 derivative of Eq. (26b) reads $\partial_{t_1}\partial_{t_2}\phi = M\partial_{t_1}\partial_m^2\mu$, which means that the cross time derivatives are not commutative [45].

For the traditional LBE models for the CHE with second order in ϵ, TE_1 and TE_2 must be removed, which gives

$$\pi_m^{(1)} = \phi u_m, \quad B_m^{(1)} = \frac{\tau_2}{\tau_1}\left[\partial_n\left(c_2^2\eta - \frac{M}{\tau_2}\right)\mu\delta_{mn} + \partial_{t_1}\pi_m^{(1)}\right]. \tag{32}$$

The mobility is commonly defined as $M = c_s^2\eta\tau$, then we get

$$B_m^{(1)} = \frac{\tau_2}{\tau_1}\partial_{t_1}(\phi u_m). \tag{33}$$

Note that if $\bar{\boldsymbol{C}} = \phi\boldsymbol{u}\boldsymbol{u}$ is retained in Eq. (10), from Eq. (28) we have $B_m^{(1)} = \tau_2/\tau_1\phi[\partial_{t_1}(u_m) + u_n\partial_n u_m]$, which is consistent with the source term in Ref. [19]. In the calculation, the t_1 derivative can be approximated by the time derivative, and the source term is defined as

$$S_i = \bar{\omega}_i C_0 + \frac{\tau_2}{\tau_1}\frac{\omega_i \boldsymbol{c}_i \cdot \partial_t(\phi\boldsymbol{u})}{c_s^2}, \tag{34}$$

where the additional introduced multiple-scale time derivative terms, such as $\partial_{t_2}(\phi\boldsymbol{u})$, $\partial_{t_3}(\phi\boldsymbol{u})$, and $\partial_{t_4}(\phi\boldsymbol{u})$, have no influence on the second-order accuracy of the recovered equation. Note that the second moment of the source term is not required to recover the above second-order CHE. In this work, our aim is to eliminate the main truncation error in $\mathrm{TE}_3 + \mathrm{TE}_4$ via carefully designing the correction term to obtain a LBE model for the CHE with improved accuracy.

Inserting Eq. (10) into Eq. (29) and using Eq. (34), TE_3 can be rewritten as

$$\mathrm{TE}_3 = c_s^2\eta\big(\tau_2^2 + 3\tau_3\big)\partial_{t_1}\partial_m^2\mu + 3c_s^2\tau_3\partial_m^2\partial_n(\phi u_n) + c_s^2\tau_1\tau_2\partial_m^2 C_0^{(1)} + \big(2\tau_2^2 + 2\tau_3\big)\partial_{t_1}^2\partial_m(\phi u_m). \tag{35}$$

Similarly, TE_4 can be rewritten as

$$\begin{aligned}\mathrm{TE}_4 = {} & \left(3\tau_4 + 5\tau_2\tau_3 + 2\tau_2^3\right)\partial_{t_1}^3\partial_m(\phi u_m) + c_s^2(12\tau_4 + 6\tau_2\tau_3)\partial_{t_1}\partial_m^2\partial_n(\phi u_n) + 3c_s^4\tau_4\eta\partial_m^2\partial_n^2\mu \\ & + \left(2\tau_2^2 + 2\tau_3\right)\left(\partial_{t_1t_2} + \partial_{t_2t_1}\right)\partial_m(\phi u_m) + c_s^2\eta\left(6\tau_4 + 4\tau_3\tau_2 + \tau_2^3\right)\partial_{t_1}^2\partial_m^2\mu + c_s^2\eta\left(\tau_2^2 + 3\tau_3\right)\partial_{t_2}\partial_m^2\mu \\ & + c_s^2\left(3\tau_1\tau_3 + \tau_1\tau_2^2\right)\partial_{t_1}\partial_m^2 C_0^{(1)} + c_s^2\tau_1\tau_2\partial_m^2 C_0^{(2)}. \end{aligned} \tag{36}$$

Combining the balance equations at different orders of ϵ, Eq. (26) together with Eqs. (34), (35), (36), and (17), we can obtain the fourth-order macroscopic equation from the LBE model,

$$\partial_t\phi + \nabla\cdot(\phi\boldsymbol{u}) = M\nabla^2\mu + \mathrm{TE}, \tag{37}$$

with

$$\begin{aligned}\mathrm{TE} = {} & \mathrm{TE}_1 + \mathrm{TE}_2 + \mathrm{TE}_3 + \mathrm{TE}_4 \\ = {} & c_s^2\eta\left(3\tau_3 + \tau_2^2\right)\partial_t\nabla^2\mu + c_s^2\eta\left(6\tau_4 + 4\tau_3\tau_2 + \tau_2^3\right)\partial_t^2\nabla^2\mu + 3c_s^2\eta\tau_4\Delta^2\mu + 3c_s^2\tau_3\Delta\nabla\cdot(\phi\boldsymbol{u}) \\ & + \left(2\tau_3 + 2\tau_2^2\right)\partial_t^2\nabla\cdot(\phi\boldsymbol{u}) + \left(3\tau_4 + 5\tau_2\tau_3 + 2\tau_2^3\right)\partial_t^3\nabla\cdot(\phi\boldsymbol{u}) + c_s^2(12\tau_4 + 6\tau_2\tau_3)\partial_t\Delta\nabla\cdot(\phi\boldsymbol{u}) \\ & + c_s^2\left(3\tau_1\tau_3 + \tau_1\tau_2^2\right)\partial_t\nabla^2 C_0 + c_s^2\tau_1\tau_2\nabla^2 C_0 + O(\epsilon^5). \end{aligned} \tag{38}$$

To identify the leading error terms, it is useful to nondimensionalize the above equation with [47]

$$\bar{L} = \frac{\boldsymbol{x}}{L_*}, \quad \bar{U} = \frac{u}{U_*}, \quad \bar{t} = t\frac{L_*}{U_*}, \quad \bar{\mu} = \frac{\mu}{|\phi_A - \phi_B|^2\beta}, \tag{39}$$

where U_* and L_* are the characteristic velocity and length, respectively. Dropping the overbar for the sake of simplicity, the resulting equation can now be rewritten as

$$\partial_t\phi + \nabla\cdot(\phi u) = \frac{1}{\mathrm{Pe}}[\nabla^2\mu + \mathrm{TE}], \tag{40}$$

with

$$\begin{aligned}\mathrm{TE} = {} & \frac{\tau_2^2 + 3\tau_3}{\tau_2^2}\mathrm{Kn}\,\mathrm{Ma}\partial_t\nabla^2\mu + \frac{6\tau_4 + 4\tau_2\tau_3 + \tau_2^3}{\tau_2^3}(\mathrm{KnMa})^2\partial_t^2\nabla^2\mu + \frac{3\tau_4}{\tau_2^3}\mathrm{Kn}^2\Delta\nabla^2\mu \\ & + \frac{3\tau_3}{\tau_2^2}\mathrm{Pe}\,\mathrm{Kn}^2\nabla^2\nabla\cdot(\phi\boldsymbol{u}) + \frac{2\tau_2^2 + 2\tau_3}{\tau_2^2}\mathrm{Pe}(\mathrm{KnMa})^2\partial_t^2\nabla\cdot(\phi\boldsymbol{u}) \\ & + \frac{3\tau_4 + 5\tau_2\tau_3 + 2\tau_2^3}{\tau_2^3}\mathrm{Pe}(\mathrm{KnMa})^3\partial_t^3\nabla\cdot(\phi\boldsymbol{u}) + \frac{12\tau_4 + 6\tau_2\tau_3}{\tau_2^3}\mathrm{Pe}(\mathrm{Kn}^3\mathrm{Ma})\partial_t\nabla^2\nabla\cdot(\phi\boldsymbol{u}) \\ & + \frac{3\tau_1\tau_3 + \tau_1\tau_2^2}{\tau_2^3}\mathrm{PeKn}^3\mathrm{Ma}\partial_t\nabla^2 C_0 + \frac{\tau_1}{\tau_2}\mathrm{PeKn}^2\nabla^2 C_0, \end{aligned} \tag{41}$$

where $\mathrm{Pe} = U_*L_*/(|\phi_A - \phi_B|^2\beta M)$ is the numerical Peclet number, $\mathrm{Kn} = c_s\tau_2/L_*$ is the Knudsen number, $\mathrm{Ma} = U/c_s$ is the Mach number, and $\mathrm{Cn} = W/L_*$ is the Cahn number. As $\mathrm{Pe} \gg 1$, $\mathrm{Ma} \ll 1$, and $\mathrm{Kn} < 1$ [48], the term $\mathrm{PeKn}^2\nabla^2\nabla\cdot(\phi\boldsymbol{u})$ is the main error affecting the numerical results. To eliminate this term, we can define the C_0 from Eq. (41) as

$$C_0 = -\frac{3\tau_3}{\tau_1\tau_2}\nabla\cdot(\phi\boldsymbol{u}). \tag{42}$$

As a result, the final source term is given by

$$S_i = -\bar{\omega}\frac{3\tau_3}{\tau_1\tau_2}\boldsymbol{u}\cdot\nabla\phi + \frac{\tau_2}{\tau_1}\omega_i\frac{\boldsymbol{c}_i\cdot\partial_t(\phi\boldsymbol{u})}{c_s^2}. \tag{43}$$

To verify the above results derived from the CE analysis with multiple-scales expansion, we have also applied the Maxwell iteration to Eq. (9) to analyze the high-order error terms (see Appendix B for details). As the Maxwell iteration needs not explicitly introduce multiple-timescale parameters, the procedure of the derivation is much more straightforward and logically clearer [34,35]. The same leading error term can be obtained, although the coefficients of some high-order terms are different for both approaches. In addition, a higher order LBE method for the CHE may also be obtained through performing the higher-order Chapman-Enskog expansion or the Maxwell iteration. However, from the dimensionless analysis above, it is found that the higher-order terms will be of the order $O(\mathrm{KnMa}, \mathrm{Kn}^2)$, which have little effect on the numerical results.

Remark I. The modified terms can be removed by setting $\tau_3 = 0$, leading to a special relaxation time $\tau_g = 1/2 + \sqrt{3}/6$. Then, the present model reduces to the model of Liang *et al.* [18]. For other relaxation times, the correction term plays an important influence on the interface.

Remark II. As all of the error terms are proportional to Kn, the value of the Knudsen number should be very small via adjusting the relaxation time to improve the accuracy of the numerical results. However, the coefficients of all the error terms are also controlled by $(\tau_g - 1/2)$, which gives rise to viscosity-type-dependent truncation errors. Hence, the value

of the relaxation time should be within a reasonable range to maintain the accuracy and stability of the LBE model.

Remark III. The form of the correction term is not unique. Without C_0, the leading error term can also be eliminated by defining the $\boldsymbol{B}^{(2)}$. From Eq. (29), the source term can be defined by

$$S_i = \frac{\omega_i \boldsymbol{c}_i}{c_s^2} \cdot \left[\frac{\tau_2}{\tau_1} \partial_t (\phi \boldsymbol{u}) + \frac{3c_s^2 \tau_3}{\tau_1} \nabla\nabla \cdot (\phi \boldsymbol{u}) \right]. \tag{44}$$

Clearly, this formula will consume more computational resources due to computing the second derivative. For simplicity, we take Eq. (43) as a demonstration.

III. NUMERICAL RESULTS AND DISCUSSION

In this section, several tests will be performed to validate the accuracy and stability of the proposed LBE model with the source term defined by Eq. (43) and the equilibrium distribution defined by Eq. (11). In Eq. (43), $\bar{\omega}_i = \omega_i$ for $i > 0$ and $\bar{\omega}_0 = \omega_0 - 1$. A comparison between the present method and the previous second-order ones for CHE proposed by Liang *et al.* [18] (labeled as LSG-LBE) and Zu and He [22] (labeled as ZH-LBE) is made. Although the LBE model for the CHE proposed by Liang *et al.* is a multiple-relaxation-time version, we only use the single-relaxation-time version of their model for a fair comparison. In addition, we take $\phi_A = -\phi_B = 1$ unless otherwise stated. The spatial gradients and Laplace operators are discretized with the isotropy central schemes [15,49]. In what follows, the dimensionless number $\mathrm{Pe} = U_0 W / (|\phi_A - \phi_B|^2 M \beta)$ is used.

TABLE I. Relative errors of the interface with different relaxation times for the diagonal translation of a circular interface at $\mathrm{Pe} = 2000$.

	$\|E(\phi)\|_{\max}$			$\|E(\phi)\|_2$		
τ_g	ZH-LBE	LSG-LBE	Present	ZH-LBE	LSG-LBE	Present
0.6	2.1526	2.1403	2.0134	2.2062	2.2068	2.0453
0.7	1.2058	1.2222	0.2301	0.4044	0.4051	0.0411
0.8	0.3285	0.3248	0.1767	0.0804	0.0797	0.0357
0.9	0.5688	0.5678	0.2098	0.1965	0.1961	0.0494
1.0		0.6269	0.2278		0.2475	0.0591
1.2	0.7283	0.8598	0.2908	0.3282	0.5847	0.0693

A. Diagonal translation of a circular interface

We consider a circular droplet motion under a constant velocity $\boldsymbol{u} = (U_0, U_0)$. Initially, a circular droplet with radius $R = L_0/5$ is placed at the center of a periodic domain of size $L_0 \times L_0$. After one period $T = L_0/U_0$, the final shape should coincide with the initial shape. In simulations, the parameters are set as $\mathrm{Pe} = 2000$, $W = 0.02L_0$, $L_0 = 200$, $U_0 = 0.02$, $\sigma = 0.01$. To quantitatively measure the accuracy among different methods, the L_2 -norm relative error is calculated by

$$\|E(\phi)\|_2 = \sqrt{\frac{\sum_{\boldsymbol{x}} |\phi(\boldsymbol{x}, nT) - \phi(\boldsymbol{x}, 0)|^2}{\sum_{\boldsymbol{x}} |\phi(\boldsymbol{x}, 0)|^2}}, \tag{45}$$

and the relative maximum error is calculated by

$$\|E(\phi)\|_{\max} = \frac{\max|\phi(\boldsymbol{x}, nT) - \phi(\boldsymbol{x}, 0)|}{|\phi_A - \phi_B|}, \tag{46}$$

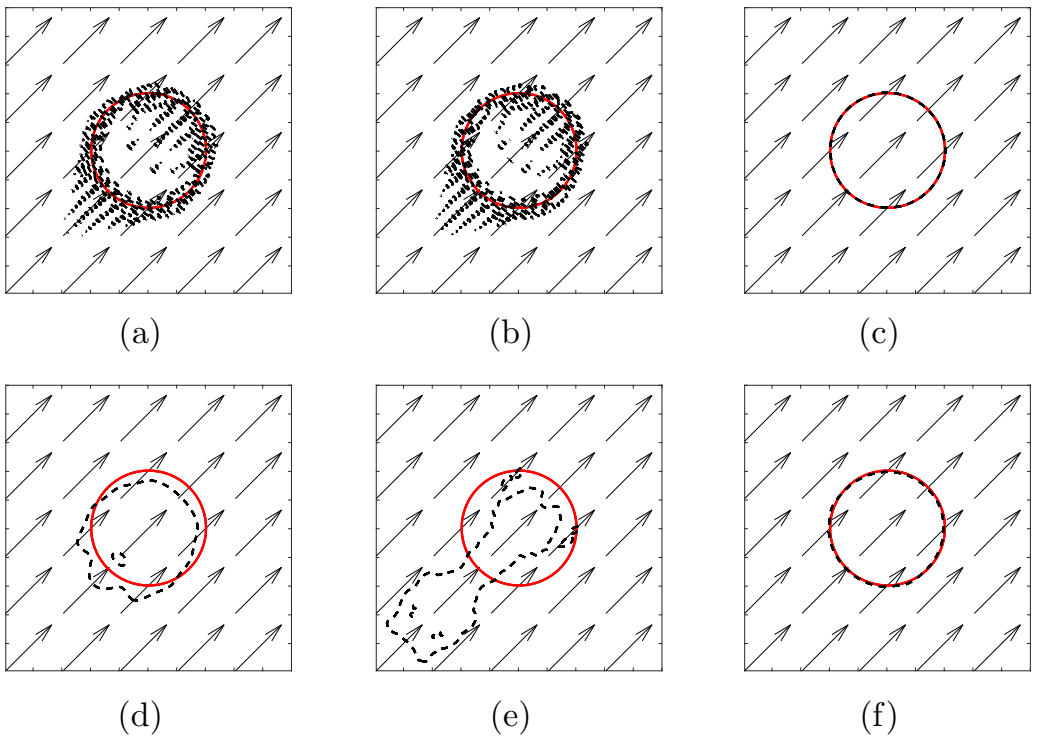

FIG. 1. The order parameter contour ($\phi = 0$) of a circular bubble under a diagonal flow at $\tau_g = 0.7$ (upper row) and $\tau_g = 1.2$ (lower row). (a,d) ZH-LBE; (b,e) LSG-LBE; (c,f) the present method. Solid: $t = 0$; dashed: $t = 10$ T.

TABLE II. Relative errors of the interface with different Pe for the diagonal translation of a circular interface.

	$\|E(\phi)\|_{\max}$			$\|E(\phi)\|_2$		
Pe	ZH-LBE	LSG-LBE	Present	ZH-LBE	LSG-LBE	Present
5		0.6456	0.1569		0.1200	0.0308
50	0.7008	0.6995	0.1313	0.1791	0.1785	0.0178
500	0.6156	0.6146	0.1954	0.1806	0.1801	0.0358
2000	0.5688	0.5678	0.2098	0.1965	0.1961	0.0494

TABLE III. Relative errors $E(\phi)$ of the interface after one period for the problem of Zalesak's disk rotation.

	$\|E(\phi)\|_{\max}$			$\|E(\phi)\|_2$		
Pe	ZH-LBE	LSG-LBE	Present	ZH-LBE	LSG-LBE	Present
5		1.0121	1.0118		0.2734	0.1777
50	0.9247	0.9248	0.4837	0.2419	0.2420	0.0658
500	0.7878	0.7878	0.2018	0.1955	0.1955	0.0476
2000	0.7692	0.7692	0.2097	0.2037	0.2037	0.0496

where $\phi(\boldsymbol{x}, 0)$ is the initial solution at position $\boldsymbol{x}$, $\phi(\boldsymbol{x}, nT)$ is the numerical result at period nT, and n is set to 10 in this simulation.

First, we test the relative errors of all the aforementioned methods with different relaxation times, and the results are shown in Table I. It can be found that the relative errors of all methods take the smallest values at $\tau_g = 0.8$, which is very close to the solution of $\tau_3 = 0$. However, for all values of the relaxation time, the present method can give the smallest error, which suggests the correction term can significantly improve the numerical accuracy. When τ_g is close to 0.5, numerical truncation errors have been severely amplified and cause inaccurate numerical results, which is consistent with the previous theoretical analysis. Then, the initial profile of the interface and its final shape with $\tau_g = 0.7$ and 1.2 are shown in Fig. 1. It is clearly seen that the final positions and shapes of the disk predicted by both the ZH-LBE method and the LSG-LBE method deviate significantly from the exact solution while those obtained by the present method agree well with the exact solutions. Finally, we calculate the relative errors of all methods with different Pe and fixed $\tau_g = 0.9$, as shown in Table II. It can be observed that the relative errors calculated by the present model are minimal for each Pe. In particular, numerical instability occurs for the ZH-LBE method when Pe = 5 while the present method can still work well, which demonstrates the improved stability of the present method.

B. Zalesak's disk rotation

The problem of Zalesak's disk is also widely used to test the capacity of numerical methods in tracking interface. As shown in Fig. 2, a circular disk with a slot is placed at the center of a periodic domain of size $L_0 \times L_0$. The disk radius and the slot width are set to be $0.4L_0$ and $0.08L_0$ in lattice units, respectively. When the velocity $\boldsymbol{u} = (u, v)$ is imposed on the computation domain ($0 \leqslant x \leqslant L_0$, $0 \leqslant y \leqslant L_0$),

$$u = -U_0\pi\left(\frac{y}{L_0} - 0.5\right), \quad v = U_0\pi\left(\frac{x}{L_0} - 0.5\right), \tag{47}$$

the disk will begin to rotate and keep its shape in the whole process. In the simulations, the parameters are set as $L_0 = 200$, $W = 0.02L_0$, $\sigma = 0.01$, Pe = 500, $U_0 = 0.02$, and $\tau_g = 0.95$. Figure 2 shows the initial shape of the disk together with the shape at $T = 10L_0/U_0$. It is clear that both the ZH-LBE method and the LSG-LBE method produce a distinct deformation at the slot while the current method still captures the interface of two phases accurately. To further give a quantitative comparison among these methods, the relative errors are calculated. It is noted that the edges of the slot of the disk are a sharp interface during initialization, which will lead to undifferentiated error values. To avoid this, the results of the finite-difference method for the above case are taken as the reference solutions, and the finite difference is introduced in the next subsection. The relative error values are shown in Table III. Again, numerical errors of the present method are minimal among all methods for each Pe.

C. Vortex deformation

We further test the capacity of the present models to capture interfacial change using a time-reversal problem [50,51]. In this test, a circular interface with radius $R = 0.15L_0$ is placed at $(0.5L_0, 0.75L_0)$ in a periodic $L_0 \times L_0$ domain. A time-dependent velocity field is given by the stream function [51,52],

$$\Psi(x, y, t) = \frac{U_0}{\pi}\sin^2\left(\frac{\pi x}{L_0}\right)\sin^2\left(\frac{\pi y}{L_0}\right)\cos\left(\frac{\pi t}{T}\right), \tag{48}$$

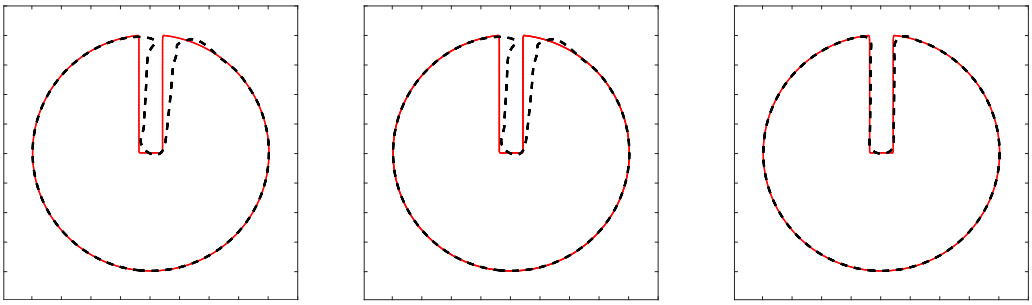

FIG. 2. Shapes of Zalesak's disk at $t = 0$ (solid) and $t = T$ (dashed). From left to right, the results are predicted by ZH-LBE, LSG-LBE, and the present method, respectively.

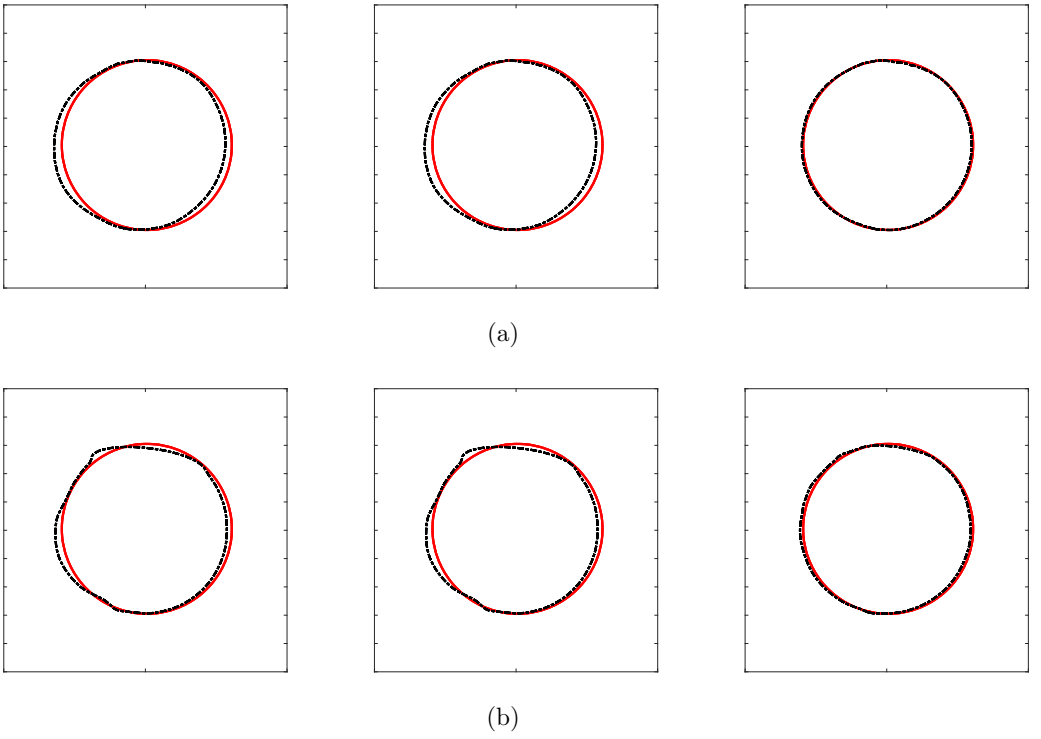

FIG. 3. The reconstructed interface $\phi = 0$ at $t = 0$ (solid) and $t = T$ (dashed line) for the single vortex field with (a) $n = 2$ and (b) $n = 4$. From left to right, the results are obtained by the ZH-LBE method, the LSG-LBE method, and the present method, respectively.

where $T = nL_0/U_0$, with n being an integer. Advected by the above velocity field, the initial circle is first stretched up to $t = T/2$, when the deformation is at a maximum, and then the velocity field will reverse, returning its initial configuration at $t = T$. In simulations, the parameters are set as $L_0 = 200$, $U_0 = 0.02$, $\sigma = 0.001$, $W = 0.01L_0$, $\tau_g = 1.2$, and Pe $= 400$. Interface contours $\phi = 0$ with $n = 2$ and 4 are shown in Fig. 3. For $n = 2$, the interface configuration predicted by all methods is similar to the initial shape. However, the locations of the interfaces predicted by both the LSG-LBE method and the ZH-LBE method deviate slightly from the initial positions. For $n = 4$, the shape of the interface predicted by all the methods is distorted. However, the present method can still restore the initial circular shape with adequate accuracy.

We also compare the results of these methods at $t = T/2$, shown in Fig. 4. Since the results of both the ZH-LBE method and the LSG-LBE method are similar, only the results obtained by the LSG-LBE method are plotted. It can be found that the initial circle is stretched into a spiral shape with a thin tail. The shapes and locations of the interface obtained by all methods are similar for $n = 2$. However, for $n = 4$, the head of the interface predicted by the present method is more

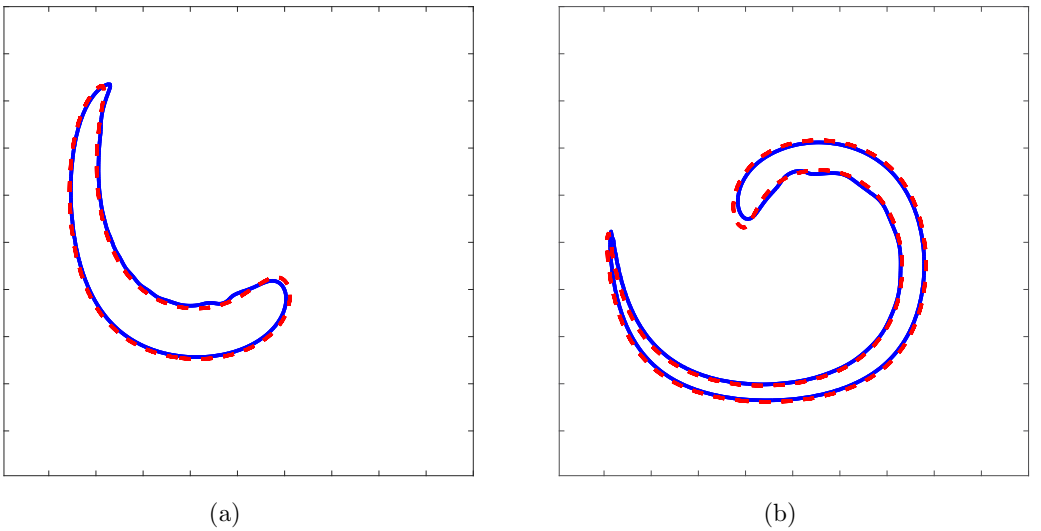

FIG. 4. The reconstructed interface $\phi = 0$ at maximum deformation at $t = T/2$ for the single vortex field with (a) $n = 2$ and (b) $n = 4$. The solid line denotes the results of the ZH-LBE/LSG-LBE method and the dotted line denotes the results of the present method.

TABLE IV. Relative errors and mass losses for the single vortex test.

	LSG-LBE			Present		
n	$\|E(\phi)\|_2$	$E(\phi)^{T/2}_{\text{area}}$	$E(\phi)^{T}_{\text{area}}$	$\|E(\phi)\|_2$	$E(\phi)^{T/2}_{\text{area}}$	$E(\phi)^{T}_{\text{area}}$
2	0.0915	0.0170	0.0050	0.0538	0.0018	0.0018
4	0.1553	0.0548	0.0071	0.0840	0.0025	0.0011

stretched. We computed the area conservation error defined as

$$E(\phi)^{T}_{\text{area}} = \frac{\sum_{\phi(\boldsymbol{x},T)>0} 1 - \sum_{\phi(\boldsymbol{x},0)>0} 1}{\sum_{\phi(\boldsymbol{x},0)>0} 1}. \tag{49}$$

The results are presented in Table IV, which suggests that the conservation property of the present method is better than that of other methods.

D. Deformation of a circular interface

In this subsection, a more complicated problem in a deformation velocity field is implemented. In this test, a circular interface with radius $R = L_0/5$ is placed in a periodic $L_0 \times L_0$ domain, and a time-dependent velocity field $\boldsymbol{u} = (u, v)$ is imposed [23],

$$u = -U_0 \sin\left[n\pi\left(\frac{x}{L_0} + 0.5\right)\right] \times \sin\left[n\pi\left(\frac{y}{L_0} + 0.5\right)\right] \cos\frac{\pi t}{T}, \tag{50a}$$

$$v = -U_0 \cos\left[n\pi\left(\frac{x}{L_0} + 0.5\right)\right] \times \cos\left[n\pi\left(\frac{y}{L_0} + 0.5\right)\right] \cos\frac{\pi t}{T}, \tag{50b}$$

where U_0 is a constant, and n is the number of vortices and is fixed at 4. T is the period and is set to be $5L_0/4U_0$. The other parameters are set as $L_0 = 500$, $\sigma = 0.01$, $U_0 = 0.025$, $\text{Pe} = 800$, $W = 4$, and $\tau_g = 1.2$. The evolutions of the interface ($\phi = 0$) obtained by all three models at $t = T/4$, $T/2$, $3T/4$, and T are shown in Fig. 5. As can be seen in Fig. 5, the initial circle undergoes a severe topological change. However, the shapes of the interface are almost identical for all models. Furthermore, to observe the thickness of the transition layer, contour lines corresponding to $\phi = -0.95$, 0, and 0.95 of numerical results are shown in Fig. 6. It can be observed that the thickness of the transition layer simulated by the present model remains compact, and the symmetry of the solutions is well-retained.

E. Binary droplet collision

In the above tests, the velocity fields are prespecified. Now we test the model with a velocity field governed by the Navier-Stokes equations. Specifically, two droplets with the same diameter D are placed $D/2$ apart in another fluid in a rectangular domain $[0, 4d] \times [0, 8d]$. The two droplets move toward each other with $V/2$ and $-V/2$, respectively, as sketched in Fig. 7. The relevant dimensionless parameters for this problem are the Weber number $\text{We} = \rho_A D V^2/\sigma$, the Reynolds number $\text{Re} = DV/\nu$, and the impact parameter $B = h/D$. Periodic boundary conditions are imposed on all boundaries. In the simulations, the parameters are $\text{We} = 60$, $\text{Re} = 200$, $B = 0.5$, $\text{Pe} = 100$, $\rho_A = \rho_B = 1$, $d = D = 60$, and $V = 0.05$. The velocity is simulated by the hydrodynamic LBE model in Ref. [18] in which the interfacial force is obtained from the phase-field equation solved by the aforementioned models. For comparison, we also solve the phase-field equation with a high-order finite-difference scheme, and the solutions are used as the reference data. Specifically, an upwind weighted essentially nonoscillatory (WENO) scheme [53] is employed to discretize the convection term, a third-order total variation diminishing Runge-Kutta scheme [54] is used for the temporal discretization, and the second-order difference scheme is applied to discretize diffusion terms. For more details, please see Refs. [54,55].

Figure 8 shows the results obtained by LSG-LBE, the present model, and the finite-difference method at $\tau_g = 0.7$ and 1. In the case of $\tau_g = 0.7$, the interface shapes obtained by all models agree well. This is because the Knudsen number proportional to the relaxation time is small and the truncation term has little effect on numerical results. In the case of

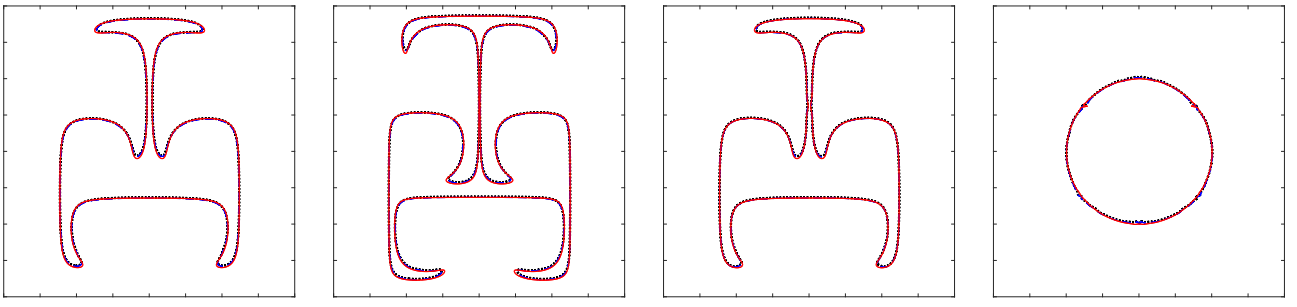

FIG. 5. The order-parameter contour ($\phi = 0$) for the deformation field problem at (a) $T/4$, (b) $T/2$, (c) $3T/4$, and (d) T. Dotted: ZH-LBE; dashed: LSG-LBE; solid: the present model.

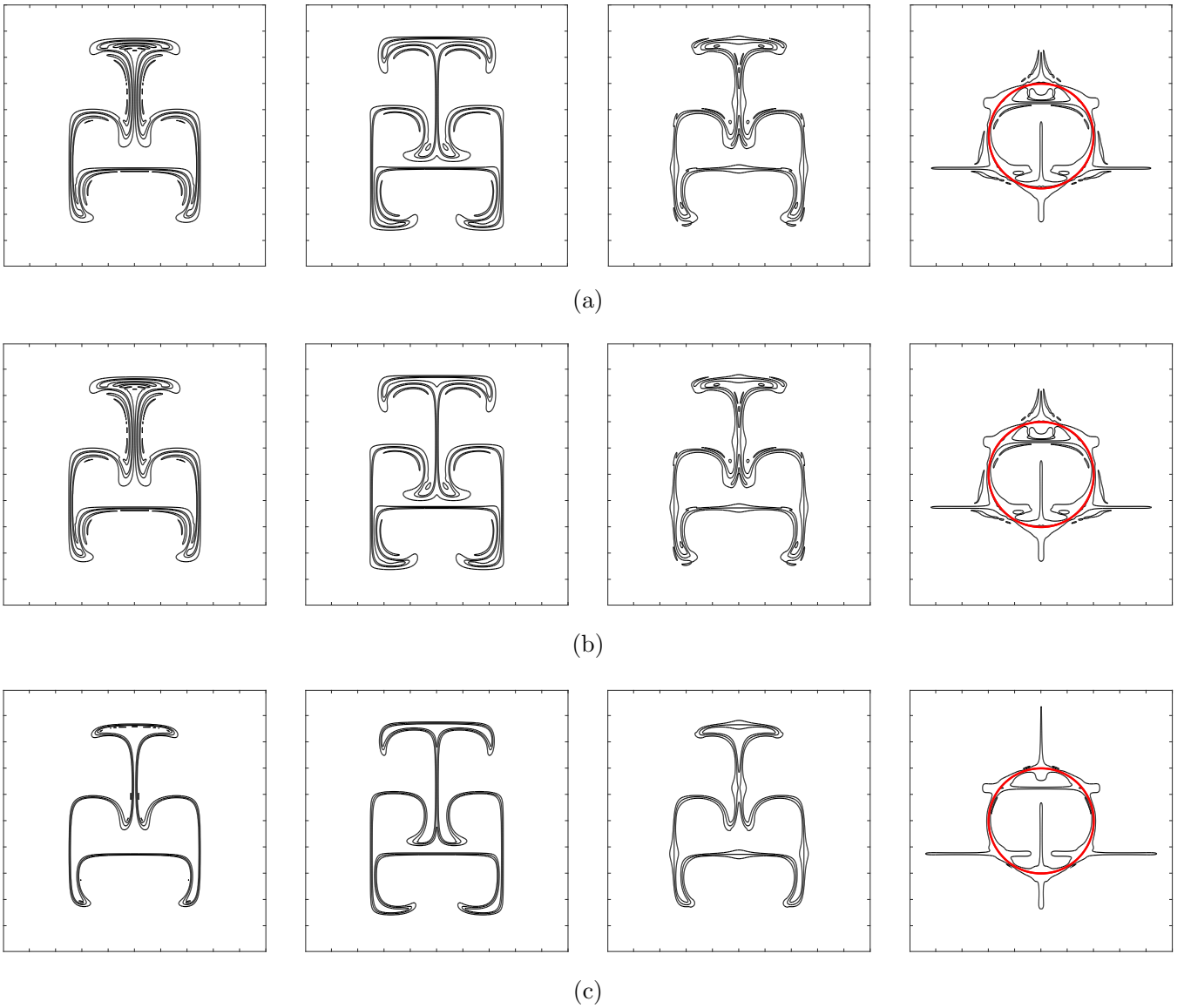

FIG. 6. The order-parameter contours ($\phi = -0.95, 0, 0.95$) predicted by (a) ZH-LBE, (b) LSG-LBE, and (c) the present model at $t = T/4,\ T/2,\ 3T/4,\ T$. The final interfaces at T against the exact solution (red thick line).

$\tau_g = 1$, differences appear in both shapes and locations of the droplets predicted by all three methods as time goes on. However, the droplet shapes predicted by the present model are much closer to the reference ones, which suggests that the correction term can improve the numerical accuracy of tracking the interface by eliminating the leading error term.

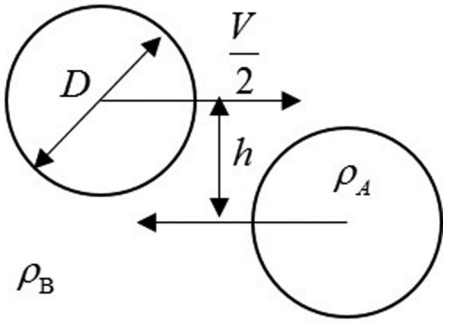

FIG. 7. Schematic of the collision of two equal-sized drops.

F. Droplet falling under gravity

Finally, we consider two falling droplets under gravity. In simulations, a smaller drop with radius R_1 is positioned at $(0.5L_0, 3L_0 - 2R_1)$ and a larger bubble with radius R_2 is placed at $(0.5L_0, 3L_0 - 2R_1 - 3R_2)$. The computational domain is set to $L_0 \times 3L_0$. Periodic boundary condition is applied to the vertical boundaries, and no-slip boundary condition is imposed on the top and bottom boundaries. The densities are $\rho_A = 2.5$ and $\rho_B = 1$. The Eötvös number defined as $\mathrm{Eo} = g(\rho_1 - \rho_2)4R_2^2/\sigma$ is set to 17. The other parameters are defined as $L_0 = 160,\ R_1 = 10,\ R_2 = 32,\ \sigma = 0.02,\ W = 3,\ v = 0.025,\ \tau_g = 0.7$. Figure 9(a) shows the evolution of the falling drops due to gravity at $\mathrm{Pe} = 10$. There are almost no

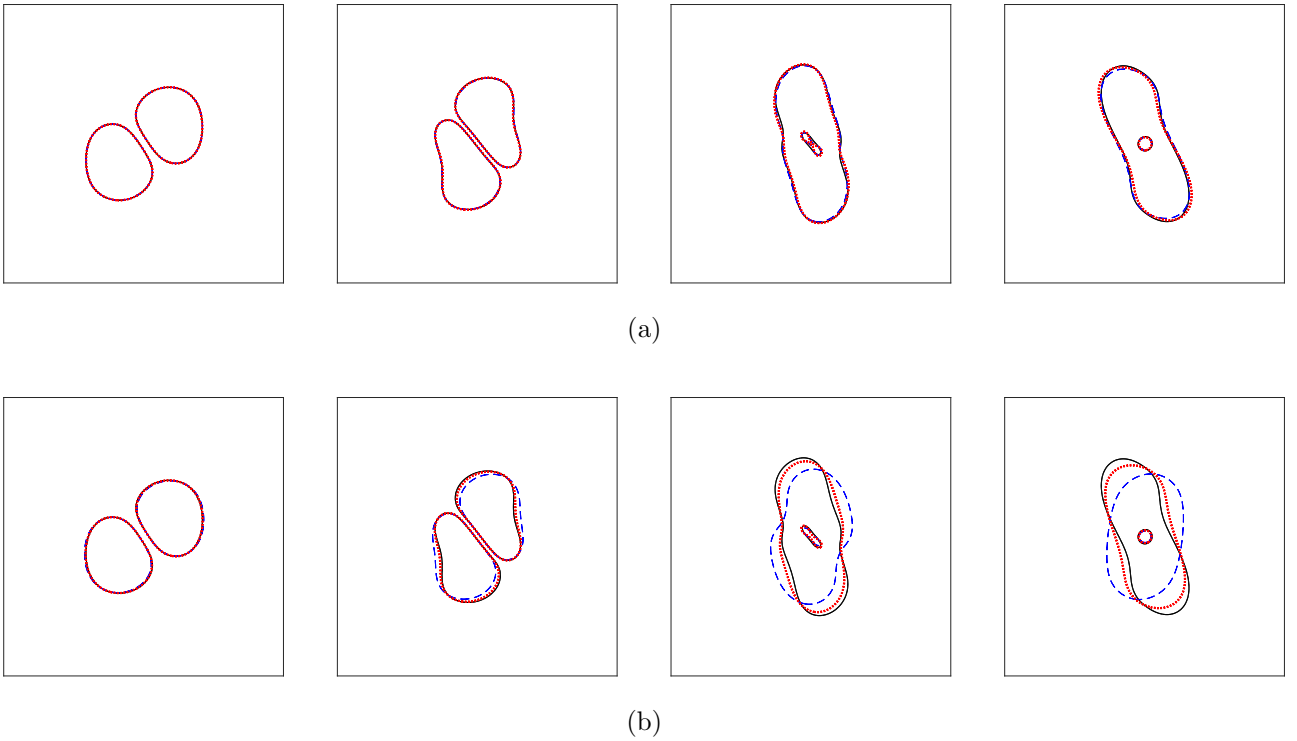

FIG. 8. Snapshots for droplet shape for (a) $\tau_g = 0.7$ and (b) $\tau_g = 1.0$. The times from the left pattern to the right are $t/10^3 = 1.2, 3, 6, 9$. Solid: the finite-difference method; dashed: LSG-LBE; dotted: the present method.

differences between the results of the LSG-LBE method and the present method for the large body. However, the position of the interface of the small drop simulated by the LSG-LBE method is lower than that predicted by the present method. This difference may be partly caused by the bulk Knudsen number of the small droplet due to the radius of the small droplet being the characteristic length. To illustrate this, we simulated the same case but with $R_2 = 20$, which suggests that a smaller bulk Knudsen number can be achieved, and the differences of the position and shape of the droplet should disappear. The results are shown in Fig. 9(b). As expected, there is little difference between the results of both methods for this case.

In addition, we repeated the above simulation with a large Pe. The results are shown in Fig. 10. The positions and the shapes of both the small droplet and the large droplet predicted by the LSG-LBE method deviate from those of the present method, which demonstrates that the correction term plays an important role in such a situation. We also found that a higher-density ratio, i.e., $\rho_A/\rho_B = 4$, can be achieved for the present model while numerical instability occurs for both the ZH-LBE model and the LSG-LBE one, which implies that the present model is able to improve the numerical stability.

IV. CONCLUSIONS

In this paper, we developed a LBE model for the Cahn-Hilliard equation. Based on the truncation error analysis of the recovered macroscopic equation, we found that the leading error term is largely determined by the Peclet number and the Knudsen number. The result is further confirmed by the Maxwell iteration. To remove the leading error term, a correction term is added in the source term. In addition, the relaxation time as a adjustable variable in the LBE model must be carefully adjusted to improve the accuracy and stability of the model. In particular, when the relaxation time τ_g is set to be a special value, i.e., $\tau_g = 1/2 + \sqrt{3}/6$, the correction term can be eliminated and the present model reduces to that of Liang [18]. For other relaxation time, the correction term can play an important role in capturing the interface accurately, especially for a large Peclet number. Several numerical tests are carried out to validate the accuracy and stability of the present model. The results show that the proposed model is capable of capturing the interface with improved accuracy and stability compared with the previous LBE models.

ACKNOWLEDGMENT

This study was supported by the National Natural Science Foundation of China (No. 51836003).

APPENDIX A: DISCRETIZATION OF THE DISCRETE VELOCITY BOLTZMANN EQUATION

In this Appendix, we shall present the discretization of the lattice Boltzmann equation with the single-relaxation-time collision operator, which can be expressed as

$$\frac{\partial h_i}{\partial t} + \boldsymbol{c}_i \cdot \nabla h_i = \Omega_i + S_i, \tag{A1}$$

where h_i is a scalar function of the particle distribution at position $\boldsymbol{x}$ and time t, satisfying $\sum_i h_i = \phi$ and $\Omega_i = (h_i^{\mathrm{eq}} -$

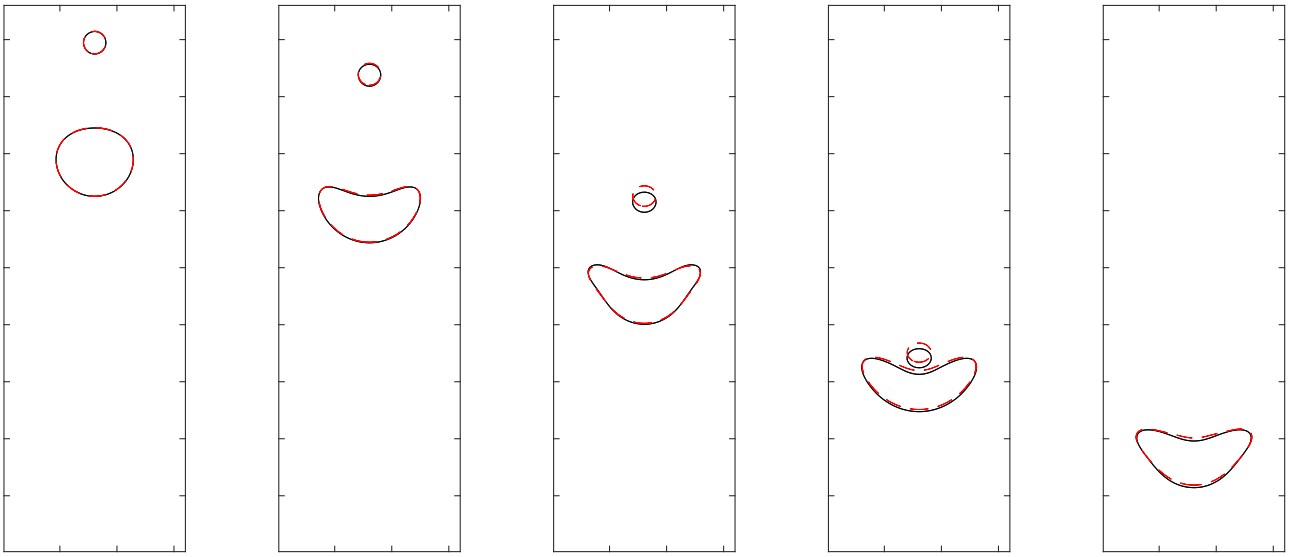

(a)

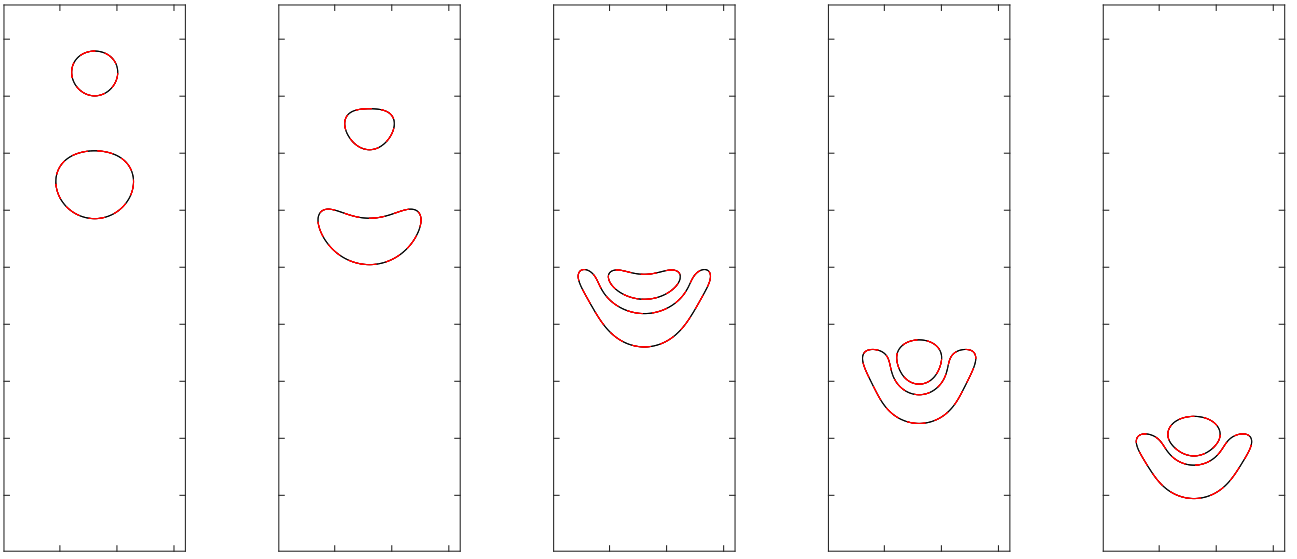

(b)

FIG. 9. Evolution of falling droplets under gravity at Pe = 10 with (a) $R_2 = 10$ and (b) $R_2 = 20$. The solid and dashed lines are the results obtained by the LSG-LBE method and the present method, respectively. From left to right, the computational times are $t/10^4 = 0.5,\ 1,\ 2,\ 3,\ 4$.

$h_i)/\tau_h$, with τ_h being the relaxation time. Integrating Eq. (A1) over a time interval $[t, t+\delta t]$ along the characteristic line $\boldsymbol{c}_i$ and applying the trapezoidal integral formula to the integral terms on the right-hand side of Eq. (A1) gives

$$h_i(x+\delta x, t+\delta t) - h_i(x,t) = \frac{\Omega_i^{t+\delta t} + \Omega_i^t}{2}\delta t + \frac{S_i^{t+\delta t} + S_i^t}{2}\delta t. \tag{A2}$$

To remove the implicity, the following variable is introduced:

$$g_i = h_i - \frac{\Omega_i}{2}\delta t - \frac{S_i}{2}\delta t. \tag{A3}$$

Inserting Eq. (A3) into Eq. (A2) gives

$$g(\boldsymbol{x}+\delta x, t+\delta t) = g(\boldsymbol{x},t) + \frac{g_i^{\mathrm{eq}} - g}{\tau_g} + \left(1 - \frac{1}{2\tau_g}\right)S_i\delta t, \tag{A4}$$

where $\tau_g\delta t = \tau_h + 0.5\delta t$ and $g_i^{\mathrm{eq}} = h_i^{\mathrm{eq}}$. From Eq. (A3), the order parameter can be calculated by

$$\phi = \sum_i g_i + \frac{\delta t}{2}\sum_i S_i. \tag{A5}$$

Note that, for the sake of derivative convenience, the coefficient $1 - 1/(2\tau_g)$ is absorbed into the source term S_i in Eq. (9).

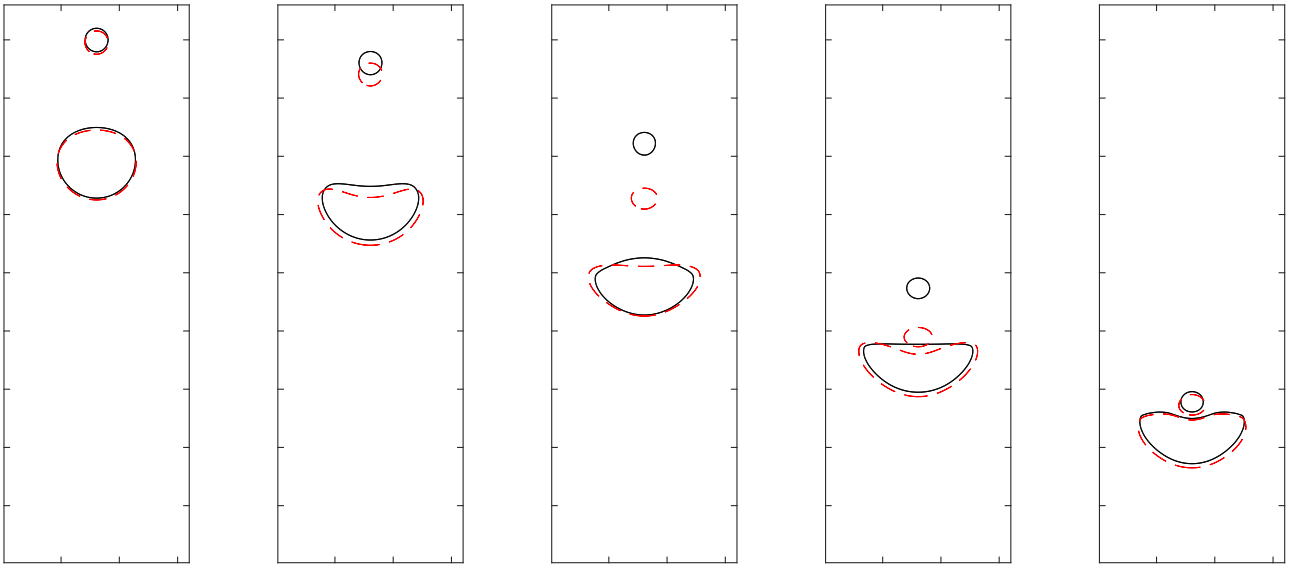

FIG. 10. Evolution of falling droplets under gravity at PE = 400. The solid and dashed lines are the results obtained by the LSG-LBE method and the present method, respectively. From left to right, the computational times are $t/10^4 = 0.5,\ 1,\ 2,\ 3,\ 4$.

In addition, the Taylor expansion of the source term $S_i(\boldsymbol{x}, t+\delta t)$ with respect to time t leads to

$$S_i(\boldsymbol{x}, t+\delta t) = S_i(\boldsymbol{x}, t) + \delta t \partial_t S_i(\boldsymbol{x}, t) + \frac{\delta t^2}{2}\partial_t^2 S_i(\boldsymbol{x}, t) + \frac{\delta t^3}{6}\partial_t^3 S_i(\boldsymbol{x}, t) + \cdots . \tag{A6}$$

With this approximation, Eq. (A2) becomes

$$h_i(\boldsymbol{x}+\delta x, t+\delta t) - \frac{\delta t}{2}\Omega_i^{t+\delta t} = h_i(x, t) - \frac{\delta t}{2}\Omega_i^t + \Omega_i^t \delta t + \tilde{S}_i \delta t, \tag{A7}$$

where $\tilde{S}_i = S_i(\boldsymbol{x}, t) + 1/2\sum_{n\geqslant 1}\frac{\delta t^n}{n!}\partial_t^n S_i(\boldsymbol{x}, t)$. To remove the implicity, an alternative variable is

$$g_i = h_i - \frac{\delta t}{2}\Omega_i. \tag{A8}$$

Inserting Eq. (A8) into Eq. (A7) leads to

$$g(\boldsymbol{x}+\delta x, t+\delta t) = g(\boldsymbol{x}, t) + \frac{g_i^{\mathrm{eq}} - g}{\tau_g} + \tilde{S}_i \delta t. \tag{A9}$$

Then, the order parameter can also be calculated by

$$\phi = \sum_i g_i. \tag{A10}$$

APPENDIX B: HIGH-ORDER ANALYSIS WITH THE MAXWELL ITERATION METHOD

In the Maxwell iteration, the time step δt is chosen as a small parameter. We still express the moments of the force term and the equilibrium function as Eqs. (14) and (10). Like the previous analysis, we first derive the moments of the force term required to match the CHE with second-order accuracy. By retaining terms to $O(\delta t^2)$ and applying the Taylor expansion to the left-hand side of Eq. (9), we have

$$-\frac{g - g^{\mathrm{eq}}}{\tau_1} + S_i = D_i g^{\mathrm{eq}} - \tau_2 D_i^2 g^{\mathrm{eq}} + \tau_1 D_i S_i + O(\delta t^2). \tag{B1}$$

Summing Eq. (B1) over i and using Eqs. (10) and (14) lead to

$$\partial_t \phi + \nabla\cdot(\phi \boldsymbol{u}) = M\nabla^2\mu + \underbrace{\tau_2\partial_t\partial_m(\phi u_m) - \tau_1\partial_m B_m}_{\mathrm{TE}_2}, \tag{B2}$$

where $M = c_s^2\eta\tau_2$. To recover the CHE up to second-order accuracy, the moments of the source term must take

$$B_m = \frac{\tau_2}{\tau_1}\partial_t(\phi u_m). \tag{B3}$$

As seen, this is consistent with the results of the CE analysis.

To analyze the truncation error of the recovered CHE, we further apply the Maxwell iteration to Eq. (9) and retain the terms to $O(\delta t^4)$,

$$D f_i^{\mathrm{eq}} = \tau_4 D^4 f_i^{\mathrm{eq}} + \tau_3 D^3 f_i^{\mathrm{eq}} + \tau_2 D^2 f_i^{\mathrm{eq}} + \tau_1\tau_3 D^3 S_i + \tau_1\tau_2 D^2 S_i - \tau_1 D S_i + O(\delta t^4). \tag{B4}$$

With the aid of Eqs. (11) and (B3), the recovered macroscopic equation can be written as

$$\partial_t\phi + \nabla\cdot(\phi\boldsymbol{u}) = M\nabla^2\mu + \mathrm{TE}, \tag{B5}$$

with the truncation error (TE)

$$\mathrm{TE} = (3\tau_4 + 3\tau_2\tau_3)\partial_t^3\nabla\cdot(\phi\boldsymbol{u}) + 3c_s^2 M\frac{\tau_4}{\tau_2}\nabla^4\mu + c_s^2(12\tau_4 + 3\tau_2\tau_3)\partial_t\Delta\nabla\cdot(\phi\boldsymbol{u}) + M\left(\frac{6\tau_4}{\tau_2} + \tau_3\right)\partial_t^2\nabla^2\mu + 2\left(\tau_2^2 + \tau_3\right)\partial_t^2\nabla\cdot(\phi\boldsymbol{u}) + M\left(\frac{3\tau_3}{\tau_2} + \tau_2\right)\partial_t\nabla^2\mu + 3c_s^2\tau_3\Delta\nabla\cdot(\phi\boldsymbol{u}) + c_s^2\tau_1\tau_2\nabla^2 C_0 + 3c_s^2\tau_1\tau_3\partial_t\nabla^2 C_0 + O(\delta t^4). \tag{B6}$$

Using Eq. (39), the dimensionless equation reads

$$\partial_t \phi + \nabla \cdot (\phi \boldsymbol{u}) = \frac{1}{\mathrm{Pe}}\left(\nabla^2 \mu + \mathrm{TE}\right), \tag{B7}$$

$$\mu = (\phi - \phi_A)(\phi - \phi_B)\left(\phi - \frac{\phi_A + \phi_B}{2}\right) - \frac{\mathrm{Cn}^2 |\phi_A - \phi_B|^2}{32}\nabla^2 \phi, \tag{B8}$$

$$\begin{aligned}\mathrm{TE} = {} & \frac{3\tau_3 + \tau_2^2}{\tau_2^2}\mathrm{KnMa}\partial_t \nabla^2 \mu + \frac{3\tau_4}{\tau_2^3}\mathrm{Kn}^2 \nabla^2 \nabla^2 \mu + \frac{6\tau_4 + \tau_2\tau_3}{\tau_2^3}(\mathrm{KnMa})^2 \partial_t^2 \nabla^2 \mu \\ & + \frac{3\tau_4 + 3\tau_3\tau_2}{\tau_2^2}\mathrm{Pe}(\mathrm{KnMa})^3 \partial_t^3 \nabla \cdot (\phi \boldsymbol{u}) + \frac{12\tau_4 + 3\tau_2\tau_3}{\tau_2^3}\mathrm{PeKn}^3\mathrm{Ma}\partial_t \Delta \nabla \cdot (\phi \boldsymbol{u}) \\ & + \frac{2\tau_2^2 + 2\tau_3}{\tau_2^2}\mathrm{Pe}(\mathrm{KnMa})^2 \partial_t^2 \nabla \cdot (\phi \boldsymbol{u}) + \frac{3\tau_3}{\tau_2^2}\mathrm{PeKn}^2 \Delta \nabla \cdot (\phi \boldsymbol{u}) + \frac{\tau_1}{\tau_2}\mathrm{PeKn}^2 \nabla^2 C_0 + \frac{3\tau_1\tau_3}{\tau_2^3}\mathrm{PeKn}^3\mathrm{Ma}\partial_t \nabla^2 C_0. \end{aligned} \tag{B9}$$

As both the Knudsen number and the Mach number are small parameters and the Peclet number may take a very large value, the above equation can be simplified by neglecting all terms of order $O(\mathrm{Kn}^2)$,

$$\partial_t \phi + \nabla \cdot (\phi \boldsymbol{u}) = \frac{1}{\mathrm{Pe}}\left[\nabla^2 \mu + \mathrm{PeKn}^2 \frac{3\tau_3}{\tau_2^2}\Delta \nabla \cdot (\phi \boldsymbol{u}) + \frac{\tau_1}{\tau_2}\mathrm{PeKn}^2 \nabla^2 C_0 + O(\mathrm{Kn}^2, \mathrm{MaKn})\right]. \tag{B10}$$

As seen, the second term on the right-hand side of the above equation is the leading error term which is consistent with the result of the Chapman-Enskog expansion.

[1] C. W. Hirt and B. D. Nichols, J. Comput. Phys. **39**, 201 (1981).
[2] M. Sussman, A. S. Almgren, J. B. Bell, P. Colella, L. H. Howell, and M. L. Welcome, J. Comput. Phys. **148**, 81 (1999).
[3] D. M. Anderson, G. B. McFadden, and A. A. Wheeler, Annu. Rev. Fluid Mech. **30**, 139 (1998).
[4] D. Jacqmin, J. Comput. Phys. **155**, 96 (1999).
[5] V. Badalassi, H. Ceniceros, and S. Banerjee, J. Comput. Phys. **190**, 371 (2003).
[6] H. Ding, P. D. Spelt, and C. Shu, J. Comput. Phys. **226**, 2078 (2007).
[7] H. W. Zheng, C. Shu, and Y. T. Chew, Phys. Rev. E **72**, 056705 (2005).
[8] J. W. Cahn and J. E. Hilliard, J. Chem. Phys. **28**, 258 (1958).
[9] M. E. Gurtin, Physica D **92**, 178 (1996).
[10] S. M. Allen and J. W. Cahn, Acta Metall. **27**, 1085 (1979).
[11] J. Shen and X. Yang, Discrete Contin. Dyn. Syst **28**, 1669 (2010).
[12] P.-H. Chiu and Y.-T. Lin, J. Comput. Phys. **230**, 185 (2011).
[13] J. Shen, X. Yang, and Q. Wang, Commun. Comput. Phys. **13**, 1045 (2013).
[14] T. Inamuro, T. Ogata, S. Tajima, and N. Konishi, J. Comput. Phys. **198**, 628 (2004).
[15] T. Lee and C.-L. Lin, J. Comput. Phys. **206**, 16 (2005).
[16] T. Lee and L. Liu, J. Comput. Phys. **229**, 8045 (2010).
[17] H. Zheng and C. Shu, J. Comput. Phys. **218**, 353 (2006).
[18] H. Liang, B. C. Shi, Z. L. Guo, and Z. H. Chai, Phys. Rev. E **89**, 053320 (2014).
[19] K. Yang and Z. Guo, Phys. Rev. E **93**, 043303 (2016).
[20] J. Y. Shao, C. Shu, H. B. Huang, and Y. T. Chew, Phys. Rev. E **89**, 033309 (2014).
[21] X. He, S. Chen, and R. Zhang, J. Comput. Phys. **152**, 642 (1999).
[22] Y. Q. Zu and S. He, Phys. Rev. E **87**, 043301 (2013).
[23] M. Geier, A. Fakhari, and T. Lee, Phys. Rev. E **91**, 063309 (2015).
[24] F. Ren, B. Song, M. C. Sukop, and H. Hu, Phys. Rev. E **94**, 023311 (2016).
[25] A. Fakhari and M. H. Rahimian, Phys. Rev. E **81**, 036707 (2010).
[26] H. L. Wang, Z. H. Chai, B. C. Shi, and H. Liang, Phys. Rev. E **94**, 033304 (2016).
[27] Y.-H. Qian and S.-Y. Chen, Phys. Rev. E **61**, 2712 (2000).
[28] B. Servan-Camas and F. T.-C. Tsai, Adv. Water Res. **31**, 1113 (2008).
[29] D. J. Holdych, D. R. Noble, J. G. Georgiadis, and R. O. Buckius, J. Comput. Phys. **193**, 595 (2004).
[30] G. Yan and J. Zhang, Math. Comput. Simul. **79**, 1554 (2009).
[31] Y. Dong, J. Zhang, and G. Yan, Appl. Math. Modell. **34**, 481 (2010).
[32] R. Huang and H. Wu, J. Comput. Phys. **327**, 121 (2016).
[33] Q. Zhai, L. Zheng, and S. Zheng, Phys. Rev. E **95**, 023313 (2017).
[34] W.-A. Yong, W. Zhao, L.-S. Luo *et al.*, Phys. Rev. E **93**, 033310 (2016).
[35] W. Zhao and W.-A. Yong, Phys. Rev. E **95**, 033311 (2017).
[36] D. Jacqmin, J. Fluid Mech. **402**, 57 (2000).
[37] J. W. Cahn and J. E. Hilliard, J. Chem. Phys. **31**, 688 (1959).
[38] Q. Li, K. H. Luo, Y. J. Gao, and Y. L. He, Phys. Rev. E **85**, 026704 (2012).
[39] Z. Guo, P. Lin, and J. S. Lowengrub, J. Comput. Phys. **276**, 486 (2014).
[40] L. Zheng, S. Zheng, and Q. Zhai, Phys. Rev. E **91**, 013309 (2015).
[41] J. Huang, C. Shu, and Y. Chew, Int. J. Numer. Methods Fluids **60**, 203 (2009).
[42] S. H. Kim and H. Pitsch, J. Comput. Phys. **303**, 19 (2015).
[43] R. Van der Sman and S. Van der Graaf, Comput. Phys. Commun. **178**, 492 (2008).
[44] Z. Guo, C. Zheng, and B. Shi, Phys. Rev. E **65**, 046308 (2002).

[45] Y.-H. Qian and Y. Zhou, Phys. Rev. E **61**, 2103 (2000).
[46] J. F. Lutsko, Phys. Rev. E **73**, 021302 (2006).
[47] S. Ansumali, I. Karlin, S. Arcidiacono, A. Abbas, and N. Prasianakis, Phys. Rev. Lett. **98**, 124502 (2007).
[48] F. Magaletti, F. Picano, M. Chinappi, L. Marino, and C. M. Casciola, J. Fluid Mech. **714**, 95126 (2013).
[49] Z. Guo, C. Zheng, and B. Shi, Phys. Rev. E **83**, 036707 (2011).
[50] W. Rider and D. Kothe (unpublished).
[51] W. J. Rider and D. B. Kothe, J. Comput. Phys. **141**, 112 (1998).
[52] Y. Sun and C. Beckermann, J. Comput. Phys. **220**, 626 (2007).
[53] G.-S. Jiang and C.-W. Shu, J. Comput. Phys. **126**, 202 (1996).
[54] G.-S. Jiang and C.-c. Wu, J. Comput. Phys. **150**, 561 (1999).
[55] J. Shao and C. Shu, Int. J. Numer. Methods Fluids **77**, 526 (2015).